

# Synthesis and structural/microstructural characteristics of antimony doped tin oxide ( $Sn_{1-x}Sb_xO_{2-\delta}$ )

Rita Singh<sup>1</sup>, Sushant Gupta<sup>2</sup> and B. Das<sup>3</sup>

<sup>1,2,3</sup>Department of Physics, University of Lucknow, Lucknow-226 007, India

<sup>1</sup>E-mail: ritasingh.singh88@gmail.com

<sup>2</sup> E-mail: sushant1586@gmail.com

<sup>3</sup>E-mail: bdas226010@gmail.com

## Abstract

Bulk samples of ( $Sn_{1-x}Sb_xO_{2-\delta}$ ) with  $x = 0.00, 0.10, 0.20, 0.30$  are synthesized by solid-state reaction route. Samples were characterized by X-ray powder diffraction (XRD), scanning electron microscopy (SEM), transmission electron microscopy (TEM) and UV-Vis spectroscopy. The x-ray diffraction patterns indicate that the gross structure/phase of ( $Sn_{1-x}Sb_xO_{2-\delta}$ ) do not change with the substitution of antimony (Sb) up to  $x = 0.30$ . The surface morphological examination with SEM revealed the fact that the grain size in the antimony doped sample is larger than that of undoped one and hence pores/voids between the grains increase with Sb concentration up to 0.30. TEM image of undoped sample indicates that the  $SnO_2$  grains have diameters ranging from 25 to 120 nm and most grains are in cubic or spherical shape. As antimony content increases, the nanocubes/spheres are converted into microcubes/spheres. The reflectance of  $Sn_{1-x}Sb_xO_{2-\delta}$  samples increases whereas absorbance of these samples decreases with the increased concentration of antimony (Sb) for the wavelength range 360 - 800 nm. The energy bandgap of Sb doped -  $SnO_2$  samples were obtained from optical absorption spectra by UV-Vis absorption spectroscopy. Upon increasing the Sb concentration the bandgap of the samples was found to increase from 3.367 eV to 3.558 eV.

## 1 Introduction

Metal oxides play a very important role in many areas of chemistry, physics, and materials science [1-6]. The unique characteristics of metal oxides make them a very diverse class of materials, with properties covering almost all aspects of materials science and solid-state physics. Oxidic materials exhibit fascinating electronic and

magnetic properties, including metallic, semiconducting, superconducting, or insulating and ferro-, ferri-, or antiferromagnetic behaviors. In technological applications, oxides are used in the fabrication of microelectronic circuits [7], capacitors [8], sensors [9], piezoelectric devices [10], fuel cells [11], semiconductors [12,13], oxygen generators [14], organic synthetics [15-19], the manufacture of engineered ceramics [20], coatings for the passivation of surfaces against corrosion [21] and as catalysts as both the support and active component [22-24]. However, nanoscale metal oxides are particularly attractive to both pure and applied researchers because of the great variety of structure and properties, especially those related to intrinsic size-dependent properties [11,24-27].

Tin (IV) dioxide (II) ( $SnO_2$ ) is one of the important members of the metal oxide family and has been extensively studied for wide range of applications such as gas sensors, transparent conductive oxides, catalysis, and far-infrared dichromic mirrors. Chemical and thermal stability, natural off stoichiometry, optical transparency and possibility of conductivity variation over a wide range makes  $SnO_2$  suitable for above mentioned applications [28].

$SnO_2$  has only one stable phase, which is known as cassiterite (mineral form) or rutile (crystal structure) with space group of  $D_4^{th}[P4_2/mnm]$ . Its unit cell contains six atoms (two tin and four oxygen), in which tin atoms occupy the center of a surrounding core composed of six oxygen atoms placed approximately at the corner of a quasi-regular octahedron (figure 1). In case of oxygen atoms, three tin atoms surround them, approximately forming an equilateral triangle. The metal atoms ( $Sn^{4+}$  cations) are located at (0,0,0) and  $(\frac{1}{2}, \frac{1}{2}, \frac{1}{2})$  positions in the unit cell and oxygen atoms ( $O^{2-}$  anions) at  $\pm(u, u, 0)$  and  $\pm(\frac{1}{2}u, \frac{1}{2}u, \frac{1}{2})$ , where the internal parameter u takes the value 0.307.

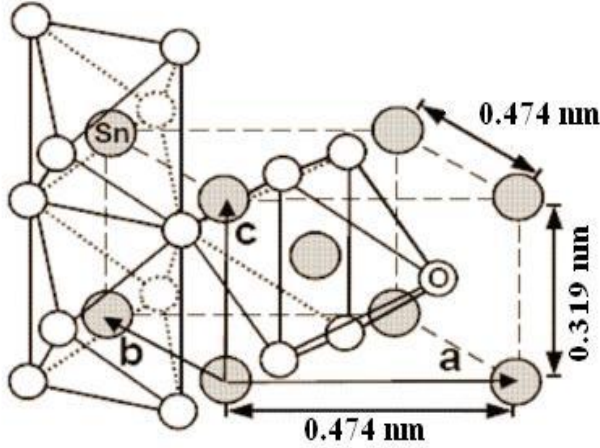


**Figure 1.** Unit cell of  $SnO_2$  with four  $O^{2-}$  anions and two  $Sn^{4+}$  cations. The crystalline structure of  $SnO_2$  is rutile: Each tin atom is at the centre of six oxygen atoms placed approximately at the corners of a regular slightly deformed octahedron and three tin atoms approximately at the corners of an equilateral triangle surround every oxygen atom.

Lattice parameters are  $a = b = 0.474$  nm and  $c = 0.319$  nm. It is a wide bandgap degenerate semiconductor with a direct band gap of approximately 3.6 eV falling in the ultra-violet region, which is an important feature for many technological applications. The valence electronic configurations of Sn and O atoms are  $5s^25p^2$  and  $2s^22p^4$ , respectively. Therefore, while forming the  $SnO_2$  molecule, the 5s and 5p electrons of the Sn atom are partially transferred to two O atoms. Each O atom can accept two electrons in its 2p orbital to form a stable octet. The energy band structure of  $SnO_2$  thus consists of a 5s conduction band and a 2p valence band separated by a forbidden gap.

In its stoichiometric form  $SnO_2$  acts as an insulator, but in its oxygen-deficient form tin dioxide behaves as an n-type semiconductor. Although the conductivity is thought to be due to intrinsic defect formation, the exact mechanism is not well understood. The bulk electronic structure has been investigated by a number of authors [29-33], although the detailed defect electronic structure has not yet been studied. Oxygen deficiency may be caused either by oxygen vacancies or tin interstitials, with reduction of some Sn(IV) ions to Sn(II) as a possible charge compensation mechanism as suggested by the observation of a SnO phase in high-resolution transmission electron microscopy (HRTEM) [34] and fine structure

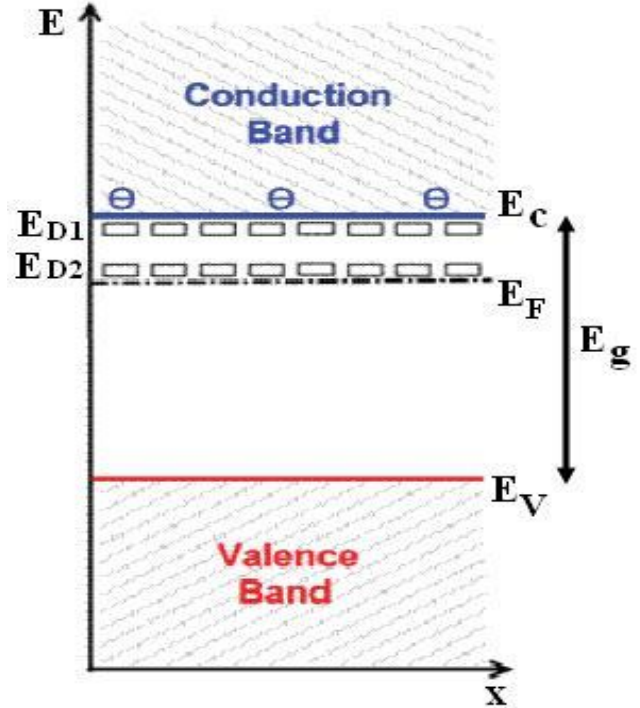


**Figure 2.** Schematic band diagram of the  $SnO_2$  bulk. Two vacancy donor levels  $E_{D1}$  and  $E_{D2}$  are located 0.03 and 0.15 eV below the conduction band ( $E_C = 0eV$ ). The bandgap ( $E_g$ ) is 3.6 eV.

emissions ascribed to Sn(II) in photoluminescence spectra [35]. Electronic conductivity could then occur due to the mobility of electrons from Sn(II) to Sn(IV) sites [36, 37].

Experimental data suggests that the cause of the non-stoichiometry in  $SnO_2$  is oxygen vacancies rather than tin interstitials. The measurement of conductivity as a function of  $O_2$  partial pressure has shown results consistent with the oxygen vacancy model [38, 39]. Electron paramagnetic resonance (EPR) studies have identified a resonance at  $g = 1.89$  associated with singly ionized oxygen vacancies ( $V_O^\cdot$  in Kröger-Vink notation) [40-42]. This resonance occurs after CO/Ar treatment of  $SnO_2$ , which results in the formation of  $V_O^\cdot$  through the interaction of CO with surface oxygen to form  $CO_2$  and neutral oxygen vacancies by the defect reaction  $CO + O_O \rightarrow CO_2 + V_O^\times$ . This forms a paramagnetic defect through the defect reaction  $V_O^\times \rightarrow V_O^\cdot + e^-$ , producing an electron in the conduction band of Sn 5s character as evidenced in EPR by a resonance at  $g = 1.99$  assigned to an unpaired electron on tin [43].  $V_O^\cdot$  is thought to transfer electrons onto tin ions to form

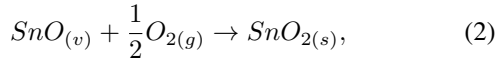
$V_{\dot{O}}$  through the reaction  $Sn_{Sn}^x + 2V_{\dot{O}} \rightarrow Sn_{Sn}'' + 2V_{\dot{O}}$ . Shallow donor levels for  $\frac{V_{\dot{O}}}{V_{\dot{O}}}$  and  $\frac{V_{\dot{O}}}{V_{\dot{O}}}$  have been identified 0.03 and 0.15 eV below the conduction band minimum (CBM), respectively (see figure 2) [38,44].

As these states lie quite close to the CBM, they will not cause a loss of transparency but will enhance the conductivity by introducing carrier electrons into the conduction band. Further evidence for the existence of these shallow states comes from cathodoluminescence studies which identified a band at 1.94 eV to result from a transition between a surface oxygen vacancy level at 1.4 eV above the valence band maximum (VBM) and a bulk shallow donor level at 0.15 eV below the CBM [44].

In this paper we report the structural, microstructural and optical properties of the bulk  $Sn_{1-x}Sb_xO_{2-\delta}$  samples with  $x = 0.00, 0.10, 0.20, 0.30$  synthesized by solid-state reaction route.

## 2 Experimental details

In the present investigation firstly the bulk  $SnO_2$  was synthesized by oxidizing the fine powder (50 mesh) of metallic tin (99.99% Aldrich chemical USA) at  $700^\circ C$  for 8 hrs in programmable temperature controlled SiC furnace. Thermal oxidation of metallic tin powder can be expressed simply by the following reactions:



In second step the as synthesized  $SnO_2$  powder was converted into form of pellets. For this we employed the most widely used technique i.e. dry pressing, which consists of filling a die with powder and pressing at  $400 \frac{Kg}{cm^2}$  into a compacted disc shape. In this way several cylindrical pellets of 2 mm thickness and 10 mm in diameter were prepared. Finally these pellets of  $SnO_2$  were put into alumina crucibles and sintered at  $900^\circ C$  in air for 8 hrs.

Similarly samples with nominal composition  $Sn_{1-x}Sb_xO_{2-\delta}$  (where  $x = 0.10, 0.20, 0.30$ ) were synthesized by standard solid-state reaction method. The appropriate ratio of the constituent oxides i.e.  $SnO_2$  (as synthesized) and  $Sb_2O_3$  (99.99% Aldrich Chemical USA) were thoroughly mixed and ground for several hours (2 to 4 hrs) with the help of mortar and pestle. The mixed powder was pressed into cylindrical pellets of 2 mm thickness and 10 mm in diameter using PVA (polyvinyl alcohol) as a binder at a pressure of  $400 \frac{Kg}{cm^2}$ . Finally the antimony doped tin oxide

**Table-1. Nominal composition and sintering condition are shown for typical samples.**

Nominal composition	Composition	Sintering conditions
$x = 0.00$	$SnO_2$	$900^\circ C$ for 8 hrs in air
$x = 0.10$	$Sn_{0.90}Sb_{0.10}O_{2-\delta}$	$1300^\circ C$ for 16 hrs in air (see fig. 3)
$x = 0.20$	$Sn_{0.80}Sb_{0.20}O_{2-\delta}$	$1300^\circ C$ for 16 hrs in air (see fig. 3)
$x = 0.30$	$Sn_{0.70}Sb_{0.30}O_{2-\delta}$	$1300^\circ C$ for 16 hrs in air (see fig. 3)

pellets were sintered in a programmable SiC furnace at  $1300^\circ C$  for 16 hrs according to the temperature profile given in figure 3. The sintering conditions employed for all the samples are given in table 1. The gross structure and

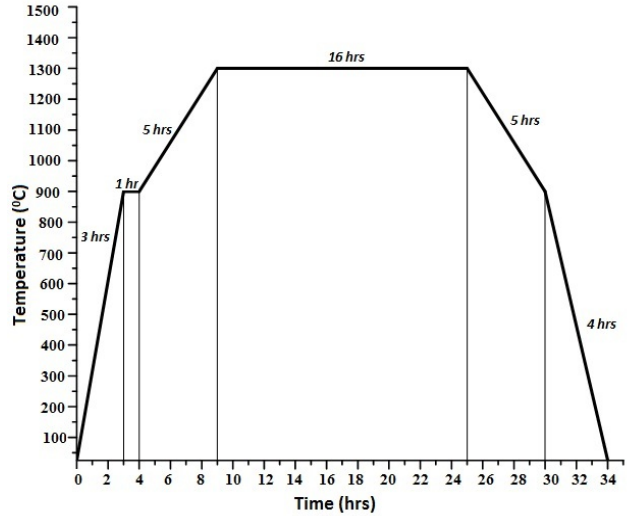


**Figure 3.** The heat treatment schedule for Sb-doped  $SnO_2$ .

phase purity of the powder sample were examined by X-ray diffraction technique. The X-ray diffraction pattern of the compounds was recorded at room temperature using X-ray powder diffractometer (18 KW Rigaku, Japan) with  $CuK_{\alpha}$  radiation ( $\lambda = 1.5418 \text{ \AA}$ ) in a wide range of Bragg angles  $2\theta (20^\circ < 2\theta < 80^\circ)$  with scanning rate of  $2^\circ \text{ min}^{-1}$ . The surface morphology of as synthesized materials has been carried out by a Joel scanning electron microscope (JSM-5600) operated at 25 KV, with a resolution of 3.5 nm.

The structural/microstructural characteristics was explored by transmission electron microscope (TEM, FEI Tecnai  $G^220$ ) in both the imaging and diffraction modes. Optical studies were performed by measuring the reflectance and the absorbance in the wavelength region 200 - 800 nm at room temperature using a Varian Cary 5000 UV-Vis spectrophotometer.

### 3 Results and discussion

Figure 4 shows the powder x-ray diffraction patterns of  $Sn_{1-x}Sb_xO_{2-\delta}$  with  $x = 0.00, 0.10, 0.20, 0.30$ . The

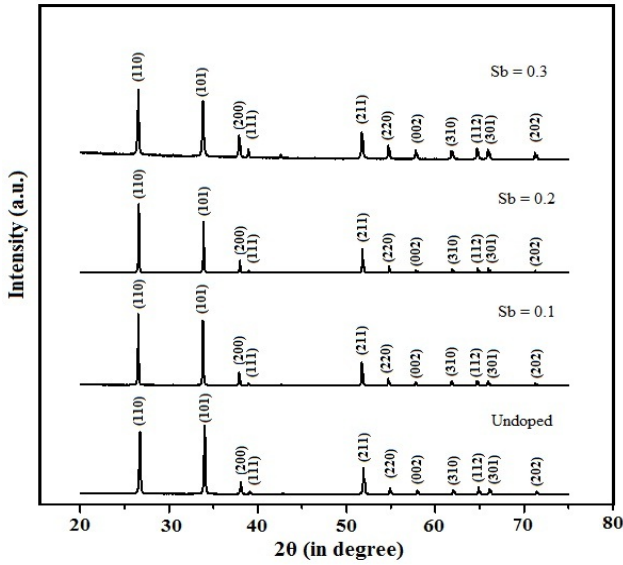


**Figure 4.** X-ray powder diffraction patterns of  $Sn_{1-x}Sb_xO_{2-\delta}$  system with  $x = 0.00, 0.10, 0.20, 0.30$ .

analysis of x-ray diffraction patterns revealed that the as synthesized doped and undoped tin oxides are pure crystalline tetragonal rutile phase of tin oxide (JCPDS card no. 041-1445) which belongs to the space group  $P4_2/mnm$  (number 136). No obvious reflection peaks from impurities, such as unreacted Sn, Sb or other oxide phases such as  $Sb_2O_5$  or  $Sb_2O_3$  are detected, indicating high purity of the product. It is perceptible from the XRD lines of figure 4 that the undoped as well as doped tin oxide samples grow along the preferred orientation of (110) and (101) reflections. The presence of other reflections such as (200), (111), (211), (220), (002), (310), (112), (301) and (202) have also been detected with considerable intensities for both doped and undoped tin oxide samples.

We have calculated the lattice parameters using high angle XRD lines such as (002), (310), (112), (301) and

**Table-2.** Lattice parameters of  $Sn_{1-x}Sb_xO_{2-\delta}$  ( $x = 0.00, 0.10, 0.20, 0.30$ )

Nominal Composition of Sb	Lattice parameters	
	$a = b$ ( $\text{\AA}$ )	$c$ ( $\text{\AA}$ )
$x = 0.00$	4.7346	3.1787
$x = 0.10$	4.7354	3.1822
$x = 0.20$	4.7360	3.1843
$x = 0.30$	4.7365	3.1899

**Table-3.** Crystallite sizes determined by XRD of undoped tin oxide sample

Diffraction line	FWHM $\beta$ (degree)	Crystallite size (nm)
110	0.1248	65.4
101	0.1440	57.7
200	0.1056	79.6
111	0.0576	146.4
211	0.1152	76.7
220	0.1056	84.8
002	0.0864	105.1
310	0.1056	87.7
112	0.1056	89.1
301	0.1248	75.9
202	0.0864	113.1

(202) shown in figure 4. The calculated lattice parameters of  $Sn_{1-x}Sb_xO_{2-\delta}$  ( $x = 0.00, 0.10, 0.20, 0.30$ ) are shown in Table 2. A small increase in the lattice parameters of the tetragonal unit cell has been observed with increasing Sb content (figure 5 & 6).

For example for  $x = 0.00$ ,  $a = 4.7346\text{\AA}$ ,  $c = 3.1787\text{\AA}$  whereas for  $x = 0.30$ ,  $a = 4.7365\text{\AA}$ ,  $c = 3.1899\text{\AA}$ . This may possibly occur due to the difference in ionic radii of  $Sn^{4+}(0.72\text{\AA})$  and  $Sb^{3+}(0.90\text{\AA})$  ions. The diffraction peaks are markedly broadened, which indicates that the crystalline sizes of samples are small. Crystallite size was automatically calculated from x-ray diffraction data using the Debye-Scherrer formula, [45]:

$$D_{hkl} = \frac{0.9\lambda}{\beta \cos \theta}, \quad (3)$$

where  $\lambda$  is the x-ray wavelength ( $1.5418\text{\AA}$  for  $CuK\alpha$ ),  $\theta$  is the Bragg angle and  $\beta$  is the full width of the diffraction line at half its maximum intensity (FWHM). The crystallite sizes were calculated (using equation 3) to be  $\sim 65, 57,$

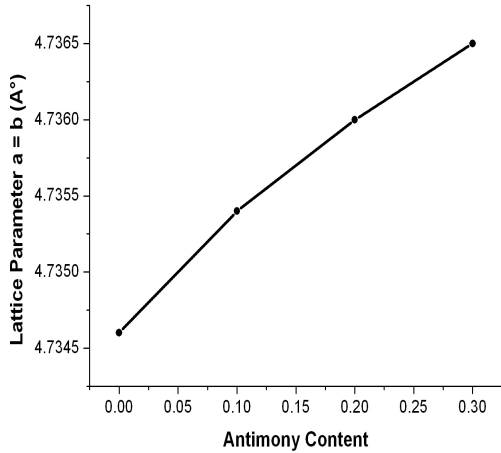


**Figure 5.** The variation of lattice parameter 'a' (or 'b') versus Sb - content shows minute elongation in lattice parameter 'a' (or 'b').

77 nm for the undoped tin oxide sample corresponding to the diffraction peaks 110, 101 and 211 respectively, as shown in Table 3. These values are in agreement with those observed by SEM and TEM investigation as will be shown later.

The scanning electron micrographs (SEM) of antimony substituted  $SnO_2$  samples are shown in figures 7 to 10. These electron micrographs reveal that the grain size in the antimony doped sample is larger than that of undoped one. In undoped sample the grains are well connected (see figure 7). When 0.10 mole of antimony is added to  $SnO_2$  sample, few pores are found between regions of well connected grains. The pores/voids between the grains also increase with antimony concentration up to 0.30 as shown in figures 8 to 10. Also we did not observe any phase aggregation other than the increase in grain size due to Sb doping. This observation obtained from SEM studies supports the XRD results.

The transmission electron micrographs (TEM) and its corresponding selected-area electron diffraction (SAED) patterns of antimony doped  $SnO_2$  samples are shown in figures 11 to 18. TEM image of undoped sample (figure 11) indicates that the  $SnO_2$  grains have diameters ranging from 25 to 120 nm and most grains are in cubic or spherical shaped. These grains size are quite similar to those calculated from Scherrer's equation 3 (see table 3). The SAED pattern shown in figure 12 taken from

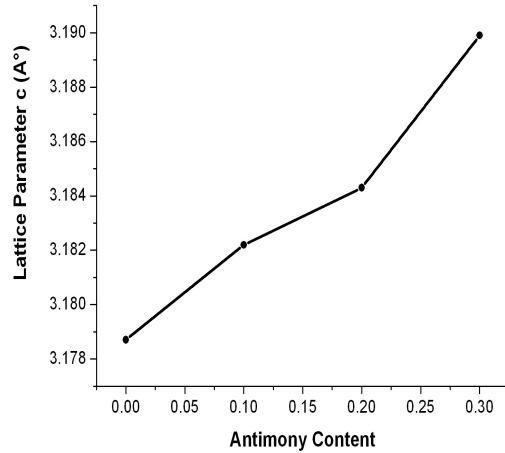


**Figure 6.** The variation of lattice parameter 'c' versus Sb - content shows minute elongation in lattice parameter 'c'.

pure  $SnO_2$  sample shows several sharp rings, which were indexed to the (110), (101), (211), and (301) planes of the rutile crystalline structure of  $SnO_2$  (JCPDS card no. 041-1445). It is clear from the TEM micrographs (figures 11 to 18) the grain size are increased (nano to micro) with increasing the Sb concentration and we get the regular SAED pattern with higher concentration of Sb element.

The optical reflectance spectra of  $Sn_{1-x}Sb_xO_{2-\delta}$  ( $x = 0.00, 0.10, 0.20, 0.30$ ) samples as a function of wavelength ranging from 200 to 800 nm is shown in figure 19. The reflectance in all four cases ( $x = 0.00, 0.10, 0.20, 0.30$ ) is small for the wavelength range 200-300 nm whereas it shows increase in reflection above the wavelength of 300 nm. The reflectance is found to increase with the increase in doping concentration.

Optical absorbance Spectra of  $Sn_{1-x}Sb_xO_{2-\delta}$  samples with different Sb concentrations ( $x = 0.00, 0.10, 0.20, 0.30$ ) is shown in figure 20. It is apparent from this figure that the absorbance increases for the wavelength range 200 - 310 nm whereas it decreases for the wavelength range 365 - 800 nm with the increase in doping concentration.

The transmittance of the as synthesized samples was calculated from reflectance (figure 19) and absorbance (figure 20) spectra using the relation:

$$T = 1 - (R + A), \quad (4)$$

where,

T = Transmittance  
R = Reflectance  
A = Absorbance.

The transmittance spectra calculated (using equation 4) for the bulk  $Sn_{1-x}Sb_xO_{2-\delta}$  ( $x = 0.00, 0.10, 0.20, 0.30$ ) samples in the wavelength range of 200 - 800 nm is shown in figure 21. The figure clearly shows the increase in transmittance due to increase in antimony (Sb) concentration for the wavelength range 360 - 800 nm whereas it shows the decrease in transmittance at the wavelength below  $\sim 305$  nm.

The variation of the optical absorption coefficient  $\alpha$  with photon energy  $h\nu$  was obtained using the absorbance data (figure 20) for various samples. The absorption coefficient  $\alpha$  may be written as a function of the incident photon energy  $h\nu$  [46]:

$$\alpha = \frac{A}{h\nu} (h\nu - E_g)^n, \quad (5)$$

where A is a constant which is different for different transitions indicated by different values of n, and  $E_g$  is the corresponding bandgap. For direct transitions  $n = \frac{1}{2}$  or  $n = \frac{2}{3}$ , while for indirect ones  $n = 2$  or 3, depending on whether they are allowed or forbidden, respectively [46]. Many groups have used the above formula to calculate the bandgap of  $SnO_2$  samples and reported that  $SnO_2$  is a direct bandgap material [47-51]. The bandgap can be deduced from a plot of  $(\alpha h\nu)^2$  versus photon energy ( $h\nu$ ). Better linearity of these plots suggests that the samples have direct band transition. The extrapolation of the linear portion of the  $(\alpha h\nu)^2$  vs.  $h\nu$  plot to  $\alpha = 0$  will give the bandgap value of the samples [52].

Figures 22 to 25 shows the  $(\alpha h\nu)^2$  versus photon energy ( $h\nu$ ) plot for pure and antimony (Sb) doped  $SnO_2$  samples. The linear fits obtained for these plots are also depicted in the figures. The bandgap ( $E_g$ ) values for the  $Sn_{1-x}Sb_xO_{2-\delta}$  samples with antimony (Sb) concentrations  $x = 0.00, 0.10, 0.20$  and  $0.30$  are 3.367 eV, 3.406 eV, 3.511 eV and 3.558 eV respectively (as shown in figures 22 to 25). From figures 22 to 25, it is observed that the bandgap of the samples increases with the increase in concentration of antimony (Sb). This is consistent with that reported in [53,54]. The bandgap is plotted as a function of increasing Sb concentration in figure 26, and also the  $E_g$  values are given in table 4. The increased of transmittance and bandgap of the as synthesized antimony doped tin oxide samples may be explained in terms of the enhancement of oxygen vacancies. Since the oxygen vacancies increase due to the partial substitution of  $Sn^{4+}$  by  $Sb^{3+}$ .

**Table-4. Grains size range and optical bandgap of the Sb doped  $SnO_2$  samples. Both grain size and optical bandgap values increases upon increasing antimony (Sb) concentration in the in the compound ( $Sn_{1-x}Sb_xO_{2-\delta}$ ).**

Nominal Composition	Bandgap ( $E_g$ (eV))	Grains Size (Range)
$x = 0.00$	3.367	Nano Range
$x = 0.10$	3.406	Micro Range
$x = 0.20$	3.511	Micro Range
$x = 0.30$	3.558	Micro Range

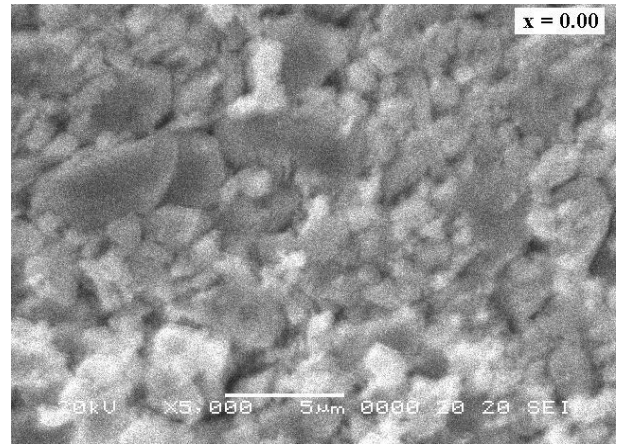


**Figure 7.** Scanning electron micrograph of the surface of the bulk  $Sn_{1-x}Sb_xO_{2-\delta}$  system with  $x = 0.00$ .

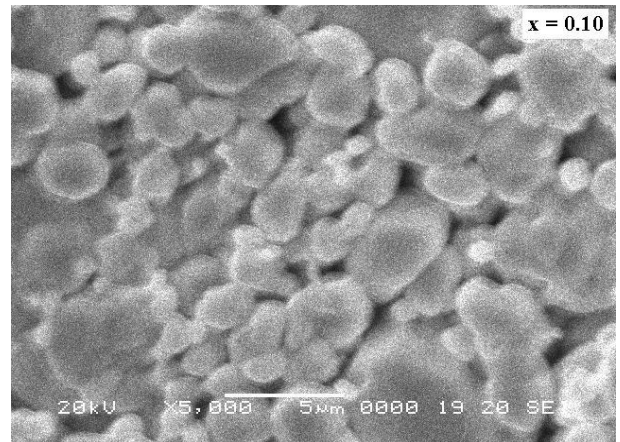


**Figure 8.** Scanning electron micrograph of the surface of the bulk  $Sn_{1-x}Sb_xO_{2-\delta}$  system with  $x = 0.10$ .

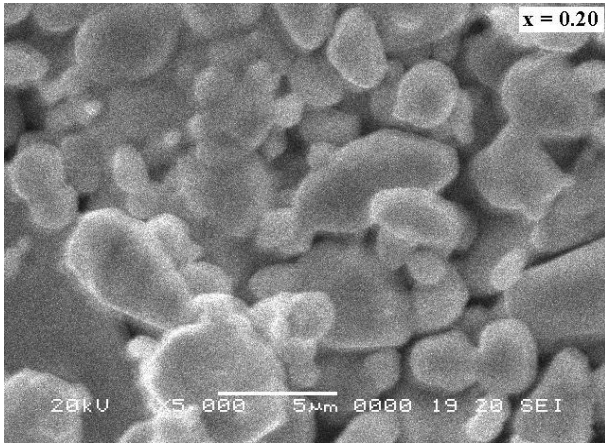


**Figure 9.** Scanning electron micrograph of the surface of the bulk  $Sn_{1-x}Sb_xO_{2-\delta}$  system with  $x = 0.20$ .

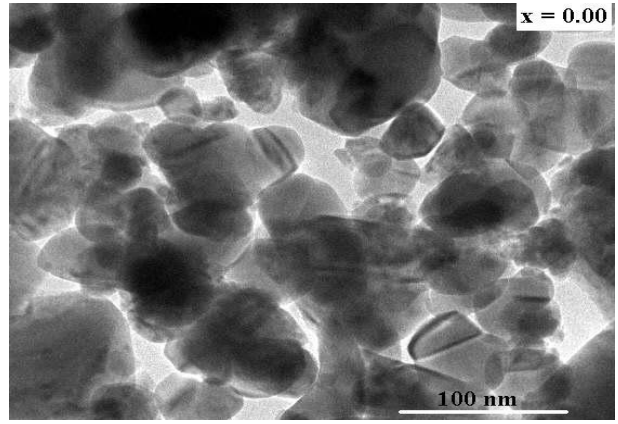


**Figure 11.** Transmission electron micrograph of the bulk  $Sn_{1-x}Sb_xO_{2-\delta}$  system with  $x = 0.00$  showing several nanocubes or nanospheres.

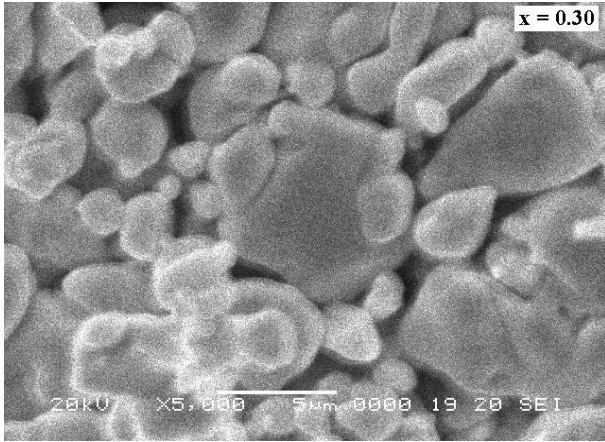


**Figure 10.** Scanning electron micrograph of the surface of the bulk  $Sn_{1-x}Sb_xO_{2-\delta}$  system with  $x = 0.30$ .

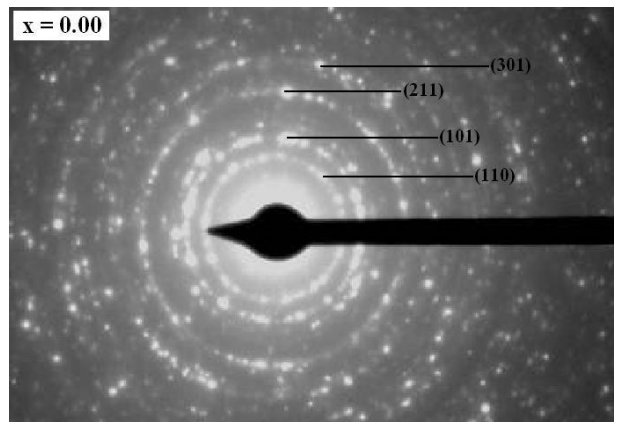


**Figure 12.** Selected area electron diffraction (SAED) pattern corresponding to figure (11) along  $[001]$  direction.

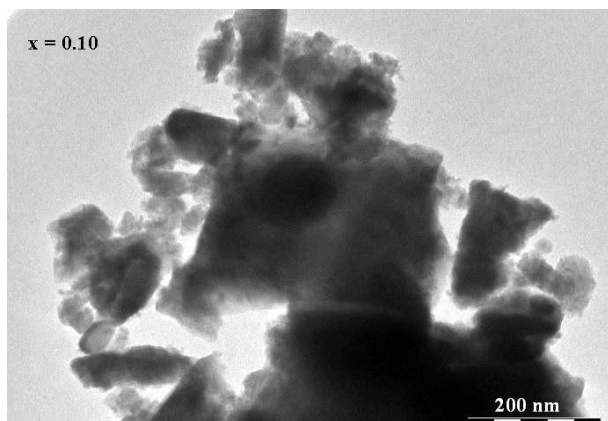


**Figure 13.** Transmission electron micrograph of the bulk  $Sn_{1-x}Sb_xO_{2-\delta}$  system with  $x = 0.10$  showing several microcrystals.

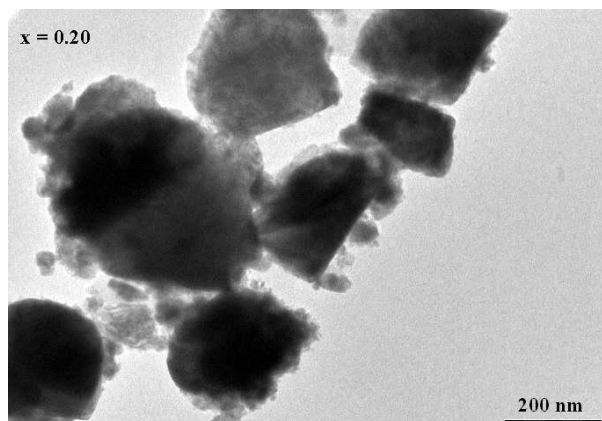


**Figure 15.** Transmission electron micrograph of the bulk  $Sn_{1-x}Sb_xO_{2-\delta}$  system with  $x = 0.20$  showing several microcrystals.

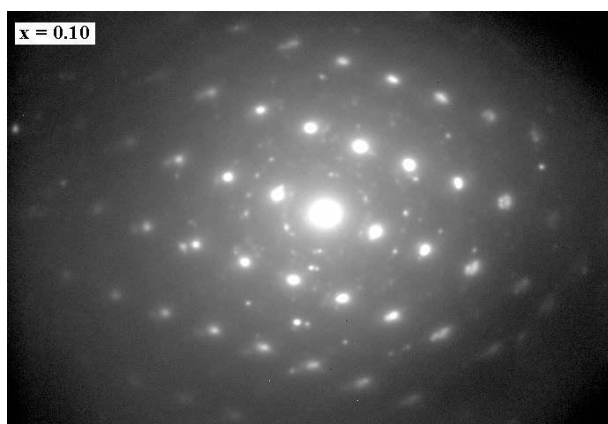


**Figure 14.** Selected area electron diffraction (SAED) pattern corresponding to figure (13) along [001] direction.

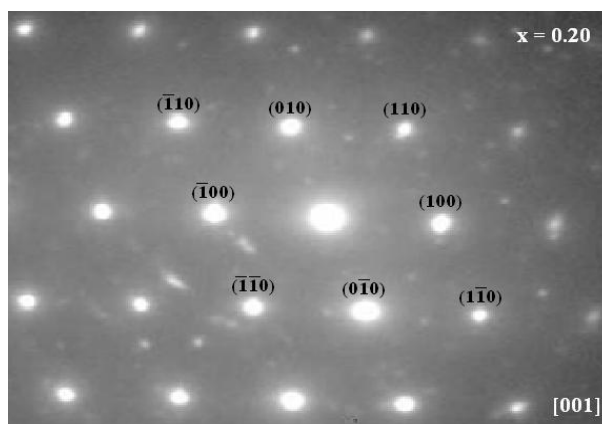


**Figure 16.** Selected area electron diffraction (SAED) pattern corresponding to figure (15) along [001] direction.

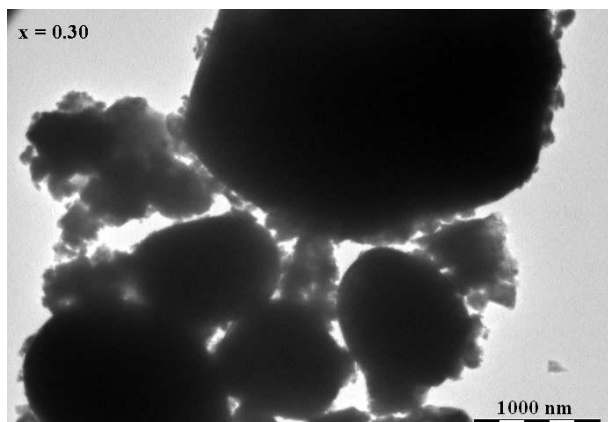


**Figure 17.** Transmission electron micrograph of the bulk  $Sn_{1-x}Sb_xO_{2-\delta}$  system with  $x = 0.30$  showing several microcrystals.

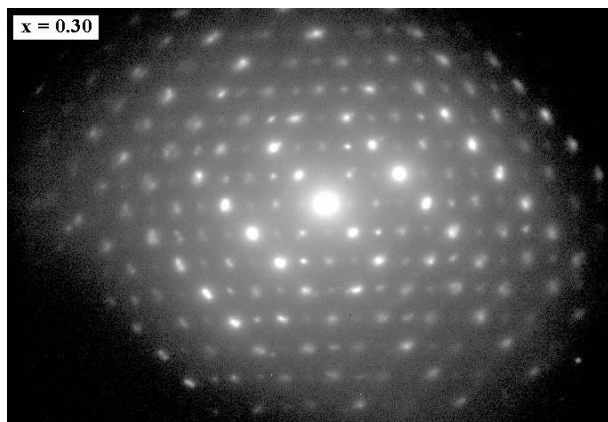


**Figure 18.** Transmission electron micrograph of the bulk  $Sn_{1-x}Sb_xO_{2-\delta}$  system with  $x = 0.30$  showing several microcrystals.

## 4 Conclusions

We have successfully prepared samples of type ( $Sn_{1-x}Sb_xO_{2-\delta}$ ) with  $x = 0.00, 0.10, 0.20$  and  $0.30$  by standard ceramic method. The analysis of x-ray diffraction patterns revealed that the as synthesized doped and undoped tin oxides are pure crystalline tetragonal rutile phase of tin oxide (JCPDS card no. 041-1445) which belongs to the space group  $P4_2/mnm$  (number 136). A small increase in the lattice parameters of the tetragonal unit cell has been observed with increasing Sb content. This possibly occurs due to the difference in ionic radii of  $Sn^{4+}$  ( $0.72\text{\AA}$ ) and  $Sb^{3+}$  ( $0.90\text{\AA}$ ) ions. The average grain size for the undoped tin oxide sample was found to be  $\sim 67$  nm as calculated by XRD using Debye Scherrer formula.

Surface morphology examination with SEM in scanning mode revealed the fact that the grains are closely packed and pores between the grains are in few numbers. These pores/voids between the grains increases with antimony concentration up to  $0.30$ . These electron micrographs also reveal that the grain size in the antimony doped sample is larger than that of undoped one.

TEM image of undoped sample indicates that the  $SnO_2$  grains have diameters ranging from  $25$  to  $120$  nm and most grains are in cubic or spherical shaped. As antimony content increases, the nanocubes/spheres are converted into microcubes/spheres.

Both reflectance and transmittance of  $Sn_{1-x}Sb_xO_{2-\delta}$  samples increases whereas absorbance of these samples decreases with the increased concentration of antimony (Sb) for the wavelength range  $360 - 800$  nm. The energy bandgap of Sb doped -  $SnO_2$  samples were obtained from optical absorption spectra by UV-Vis absorption spectroscopy. Upon increasing the Sb concentration the bandgap of the samples was found to increase from  $3.367$  eV to  $3.558$  eV.

## Acknowledgement

The authors gratefully acknowledge Dr. Alok Kumar, GSI Lucknow for providing facility of XRD and Dr. Jitendra Kumar of IIT Kanpur for his help in recording the optical spectra. Authors also thank Dr. N. P. Lalla and Dr. D. M. phase of UGC-DAE Consortium for Scientific Research Center, Indore for TEM and SEM observations. Finally, we would like to thank Prof. M. K. Mishra, Vice-chancellor and Prof. U. D. Mishra, Head, Department of Physics, University of Lucknow for their encouragement and support for providing the facilities for material synthesis.

## References

- [1] R. W. G. Wyckoff, Inorganic Compounds  $RX_n$ ,  $R_nMX_2$ ,  $R_nMX_3$ , 2nd ed. (Interscience Publishers, New York, 1964).

- [2] A. F. Wells, *Structural Inorganic Chemistry*, 6th ed. (Oxford University Press, Oxford, UK, 1987).
- [3] W. A. Harrison, *Electronic Structure and the Properties of Solids: the Physics of the Chemical Bond* (Dover Publications, New York, 1989).
- [4] H. H. Kung, *Transition Metal Oxides: Surface Chemistry and Catalysis* (Elsevier, Amsterdam, Netherlands, 1989).
- [5] V. E. Henrich and P. A. Cox, *The Surface Science of Metal Oxides* (Cambridge University Press, Cambridge, UK, 1994).
- [6] C. Noguera, *Physics and Chemistry at Oxide Surfaces* (Cambridge University Press, 1996).
- [7] J. P. Colinge, K. Hashimoto, T. Kamins, S. Y. Chiang, E. D. Liu, S. S. Peng, and P. Rissman, *Ieee Electron Device Lett.* **7**, 279 (1986).
- [8] V. Srinivasan and J. W. Weidner, *J. Electrochem. Soc.* **144**, L210 (1997).
- [9] J. Watson, *Sens Actuators* **5**, 29 (1984).
- [10] B. Noheda, *Curr. Opin. Solid-State Mater. Sci.* **6**, 27 (2002).
- [11] K. Eguchi, T. Setoguchi, T. Inoue, and H. Arai, *Solid State Ionics* **52**, 165 (1992).
- [12] C. C. Hsu and N. L. Wu, *J. Photochem. Photobiol. A* **172**, 269 (2005).
- [13] S. Lindroos and M. Leskela, *Int. J. Inorg. Mater.* **2**, 197 (2000).
- [14] D. Golberg, Y. Bando, K. Fushimi, M. Mitome, L. Bourgeois, and C. C. Tang, *J. Phys. Chem. B* **107**, 8726 (2003).
- [15] K. Nakagawa, T. Nakata, and R. Konaka, *J. Org. Chem.* **27**, 1597 (1962).
- [16] K. Nakagawa and T. Tsuji, *Chem. Pharm. Bull.* **11**, 296 (1963).
- [17] K. Nakagawa, J. Sugita, and K. Igano, *Chem. Pharm. Bull.* **12**, 403 (1964).
- [18] K. Nakagawa, J. Sugita, and H. Onoue, *Chem. Pharm. Bull.* **12**, 1135 (1964).
- [19] C. Pierlot, V. Nardello, J. Schrive, C. Mabile, J. Barbillat, B. Sombret, and J. M. Aubry, *J. Org. Chem.* **67**, 2418 (2002).
- [20] C. G. Levi, J. Y. Yang, B. J. Dalglish, F. W. Zok, and A. G. Evans, *J. Am. Ceram. Soc.* **81**, 2077 (1998).
- [21] A. Nazeri, P. P. TrzaskomaPaulette, and D. Bauer, *J. Sol-Gel Sci. Technol.* **10**, 317 (1997).
- [22] Z. R. Tian, W. Tong, J. Y. Wang, N. G. Duan, V. V. Krishnan, and S. L. Suib, *Science* **276**, 926 (1997).
- [23] I. E. Wachs, *Catal. Today* **27**, 437 (1996).
- [24] G. C. Bond and S. F. Tahir, *Appl. Catal.* **71**, 1 (1991).
- [25] Z. L. Wang, *Annu. Rev. Phys. Chem.* **55**, 159 (2004).
- [26] M. Fernandez-Garcia, A. Martinez-Arias, J. C. Hanson, and J. A. Rodriguez, *Chem. Rev.* **104**, 4063 (2004).
- [27] M. E. Franke, T. J. Koplin, and U. Simon, *Small* **2**, 36 (2006).
- [28] N. Barsan, D. Koziej, and U. Weimar, *Sens. Actuators B* **121**, 18 (2007).
- [29] P. Barbarat, S. F. Matar, and G. LeBlvenec, *J. Mater. Chem.* **7**, 2547 (1997).
- [30] M. Calatayud, J. Andres, and A. Beltran, *Surf. Sci.* **430**, 213 (1999).
- [31] L. A. Errico, *Physica B* **389**, 140 (2007).
- [32] M. A. Maki-Jaskari and T. T. Rantala, *Phys. Rev. B* **64**, 075407 (2001).
- [33] J. Robertson, K. Xiong, and S. J. Clark, *Thin Solid Films* **496**, 1 (2006).
- [34] D. Maestre, J. Ramirez-Castellanos, P. Hidalgo, A. Cremades, J. M. Gonzalez-Calbet, and J. Piqueras, *Eur. J. Inorg. Chem.*, 1544 (2007).
- [35] F. Ming, T. Xiaoli, C. Xueli, Z. Lide, L. Peisheng, and J. Zhi, *J. Phys. D: Appl. Phys.* **40**, 7648 (2007).
- [36] C. A. Vincent, *J. Electrochem. Soc.* **119**, 515 (1972).
- [37] B. Alterkop, N. Parkansky, S. Goldsmith, and R. L. Boxman, *J. Phys. D* **36**, 552 (2003).
- [38] S. Samson and C. G. Fonstad, *J. Appl. Phys.* **44**, 4618 (1973).
- [39] J. Maier and W. J. Gopel, *Solid State Chem.* **72**, 293 (1988).
- [40] P. Dinola, F. Morazzoni, R. Scotti, and D. Narducci, *J. Chem. Soc., Faraday Trans.* **89**, 3711 (1993).
- [41] F. Morazzoni, C. Canevali, N. Chiodini, C. Mari, R. Ruffo, R. Scotti, L. Armelao, E. Tondello, L. Depero, and E. Bon-tempi, *Mater. Sci. Eng., C* **15**, 167 (2001).
- [42] S. H. Sun, G. W. Meng, G. X. Zhang, T. Gao, B. Y. Geng, L. D. Zhang, and J. Zuo, *Chem. Phys. Lett.* **376**, 103 (2003).
- [43] R. Ningthoujam, D. Lahiri, V. Sudarsan, H. K. Poswal, S. K. Kulshreshtha, S. M. Sharma, B. Bhushan, and M. D. Sastry, *Mater. Res. Bull.* **42**, 1293 (2007).
- [44] J. D. Prades, J. Arbiol, A. Cirera, J. R. Morante, M. Avella, L. Zanotti, E. Comini, G. Faglia, and G. Sberveglieri, *Sensor Actuat. B* **126**, 6 (2007).
- [45] X. C. Yang, *Mater. Sci. Eng. B* **93**, 249 (2002).
- [46] J. Tauc, R. Grogorovici and A. Vancu, *Phys. Stat. Solidi.* **15**, 627 (1966).
- [47] T. Arai, *J. Phys. Soc. Japan* **15**, 916 (1960).
- [48] D. Frohlich and R. Kenkies, *Phys. Rev. Lett.* **41**, 1750 (1978).
- [49] F. Gu, S. F. Wang, M. K. Lu, X. F. Cheng, S. W. Liu, G. J. Zhou, D. Xu, and D. R. Yuan, *J. Cryst. Growth* **262**, 182 (2004).
- [50] A. E. De Souza, S. H. Monteiro, C. V. Santilli, and S. H. Pulcinelli, *J. Mater. Sci.: Mater. Electron.* **8**, 265 (1997).
- [51] E. R. Leite, M. Ines, B. Bernardi, E. Longo, J. A. Varela, and C. A. Paskocimas, *Thin Solid Films* **449**, 67 (2004).
- [52] S. Tsunekawa, T. Fukuda, and A. Kasuya, *J. Appl. Phys.* **87**, 1318 (2000).
- [53] E. Burstein, *Phys. Rev.* **93**, 632 (1954).
- [54] T. S. Möss, *Proc. Phys. Soc. Lond. Ser. B* **67**, 775 (1954).

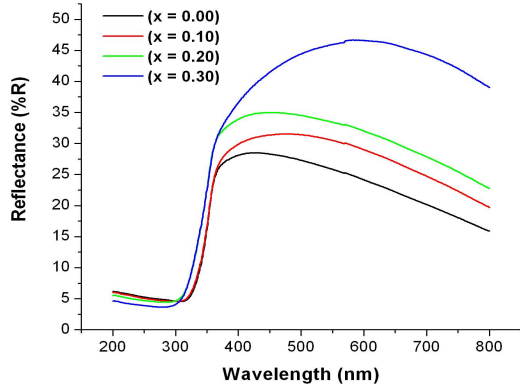


**Figure 19.** UV-Vis reflectance spectra of  $Sn_{1-x}Sb_xO_{2-\delta}$  system with  $x = 0.00, 0.10, 0.20$  and  $0.30$ .

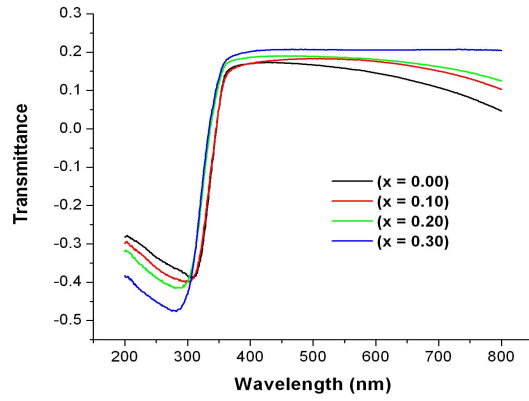


**Figure 21.** Optical Transmittance spectra (calculated from equation 4) of  $Sn_{1-x}Sb_xO_{2-\delta}$  system with  $x = 0.00, 0.10, 0.20$  and  $0.30$ .

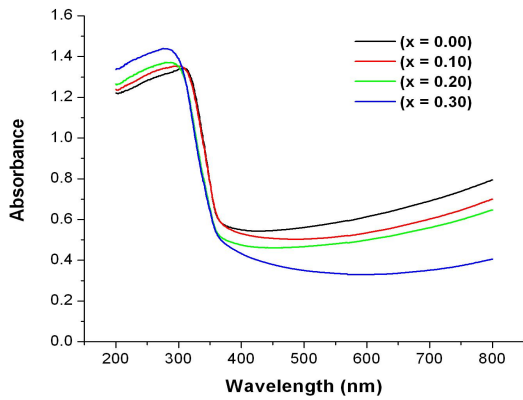


**Figure 20.** UV-Vis absorbance Spectra of  $Sn_{1-x}Sb_xO_{2-\delta}$  system with  $x = 0.00, 0.10, 0.20$  and  $0.30$ .

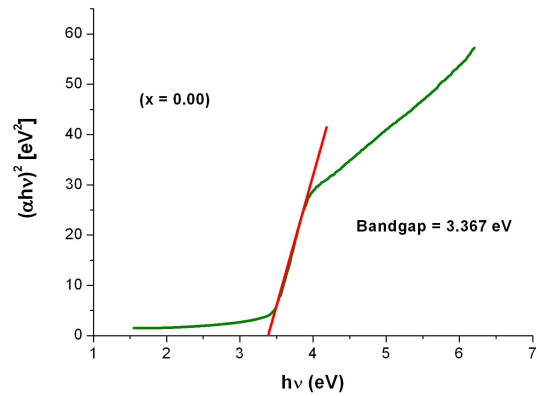


**Figure 22.**  $(\alpha h\nu)^2 [eV^2]$  versus photon energy  $(h\nu) [eV]$  curve for the bulk  $Sn_{1-x}Sb_xO_{2-\delta}$  system with  $x = 0.00$ . The direct energy bandgap  $E_g$  is obtained from the extrapolation to  $\alpha = 0$ .

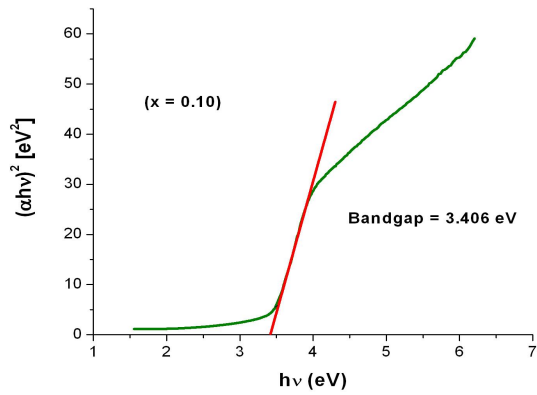


**Figure 23.**  $(\alpha h\nu)^2$  [ $eV^2$ ] versus photon energy ( $h\nu$ ) [eV] curve for the bulk  $Sn_{1-x}Sb_xO_{2-\delta}$  system with  $x = 0.10$ . The direct energy bandgap  $E_g$  is obtained from the extrapolation to  $\alpha = 0$ .

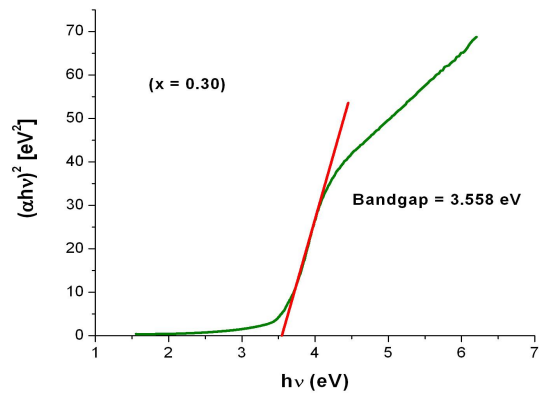


**Figure 25.**  $(\alpha h\nu)^2$  [ $eV^2$ ] versus photon energy ( $h\nu$ ) [eV] curve for the bulk  $Sn_{1-x}Sb_xO_{2-\delta}$  system with  $x = 0.30$ . The direct energy bandgap  $E_g$  is obtained from the extrapolation to  $\alpha = 0$ .

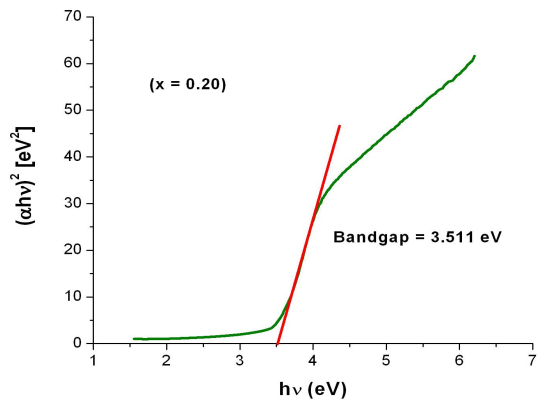


**Figure 24.**  $(\alpha h\nu)^2$  [ $eV^2$ ] versus photon energy ( $h\nu$ ) [eV] curve for the bulk  $Sn_{1-x}Sb_xO_{2-\delta}$  system with  $x = 0.20$ . The direct energy bandgap  $E_g$  is obtained from the extrapolation to  $\alpha = 0$ .

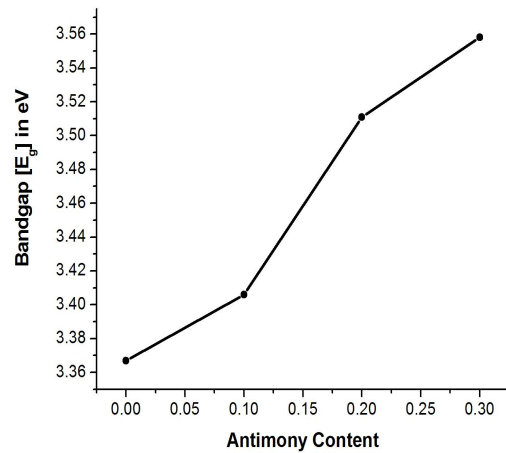


**Figure 26.** Variation of bandgap ( $E_g$ ) as a function of increasing antimony (Sb) concentration. The bandgap of the samples increased from 3.367 to 3.558 eV due to Sb doping.